

Finite-element state estimation for air-quality monitoring using wireless sensors

G. Battistelli, L. Chisci, N. Forti, G.A. Manduzio, G. Gualtieri

Abstract—This paper addresses high-resolution air quality monitoring in an urban environment exploiting data assimilation techniques that combine mathematical modeling of the pollutant dispersion dynamics along with pointwise-in-time-and-space pollutant concentration measurements provided by appropriate sensors deployed over the region of interest. In particular, the work has led to the development of a data-assimilation system and to its pilot application to air quality monitoring of a given area in the city of Florence. The developed system exploited the following ingredients: Advection-Diffusion-Reaction (ADR) Partial Differential Equation (PDE) for air pollution modeling; Finite Element Method (FEM) for spatial discretization of the ADR PDE into a finite-dimensional large-scale continuous-time state-space model; time-discretization to obtain a discrete-time state space model; use of meteo and vehicular traffic data for tuning the model parameters and computing input emissions; Ensemble Kalman Filter (EnKF) for computationally efficient data-assimilation with a large-scale model; low-cost mobile and/or fixed AirQino boards, developed by IBIMET-CNR, for measuring concentrations of several pollutants and air temperature as well as radio transmitting geolocated measurements to the data assimilation center. The effectiveness of the system, in terms of accurate space-time reconstruction of the pollutant concentration map, has been successfully tested via both computer-simulated and real data, the latter having been collected through data-acquisition campaigns with fixed and/or mobile sensors located in the area of interest.

Index Terms—State estimation; finite-element method; ensemble Kalman filter; air-quality monitoring.

I. INTRODUCTION

Most metropolitan areas, including Florence, are facing increasing environmental challenges ranging from air quality and water management to emergencies caused by climate-related hazards. In particular, air pollution is a public health issue associated with various health effects, including cardiovascular and respiratory diseases, cancer, pregnancy complications and even death [6], [10]. In a recent study the Lancet Commission on Pollution and Health, involving more than 40 international health and environmental authors, states that air pollution caused 6.5 million heart and lung-related deaths [6], [2]. Among these deaths, around 2.1 and 0.47 million are due to the actions of fine particulate (PM) and ozone (O_3) [6], [7]. In Europe, over the past decades, due to the effective legislation, many air pollutants have substantially decreased, resulting in an improved air quality across the region. However, air pollutant concentrations are still too high, and the air quality problems persist. There are various

G. Battistelli, L. Chisci, N. Forti and G.A. Manduzio are with Dipartimento di Ingegneria dell'Informazione, Università degli Studi di Firenze, Firenze, Italy. e-mail: giorgio.battistelli@unifi.it, luigi.chisci@unifi.it.

G. Gualtieri is with Institute of Biometeorology (IBIMET) of CNR, Firenze, Italy. e-mail g.gualtieri@ibimet.cnr.it

sources, activities or factors that are responsible for releasing pollutants into the atmosphere. Pollutant emitting sources can be divided into two major categories: (1) natural, e.g. forest fires, erupting volcanoes, Sahara dust, and gases released from the radioactive decay of rocks; (2) anthropogenic, e.g. road vehicles and engines, electric utilities, heating plants, industrial processes. Air pollutant composition may greatly vary as well, depending on the season, the weather and the type and number of sources. Substances emitted into the atmosphere can be gases (CO , NO , NO_2 , SO_X , O_3), or solid particles (e.g. aerosol and metals). Based on the chemical characteristics, they can be subdivided into inorganic substances¹ (minerals: silica, asbestos, metals; not minerals: CO , CO_2 , NO_X , SO_X , O_3), and organic substances (organometallic and organochlorinated compounds). This characterization leads to further classify air pollutants as: (1) primary pollutants, directly emitted from the sources (primary component of particulate matter PM, SO_X , NO , primary component of NO_2 , CO , IPA, unburned hydrocarbons, metals); secondary pollutants, chemicals species formed through reactions in the atmosphere (secondary component of particulate matter PM, O_3 , secondary component of NO_2). Many types of chemical reactions in the atmosphere create, modify, and destroy chemical pollutants. Inert pollutants, once emitted from sources, are subject to various atmospheric processes, including advection due to wind, diffusion due to atmospheric turbulence (dilution or mixing), and (dry or wet) ground deposition.

Air pollution is characterized by non uniform trends, particularly in dense urban areas, which imply the necessity for carrying out pollution monitoring at finer resolution. A fundamental step towards the improvement of the urban environment is the development of an efficient environmental monitoring system providing timely and reliable information, also in support of decision-making. As a matter of fact, traditional air quality monitoring systems rely on data collected from few expensive sensor stations and, hence, cannot provide detailed information on the distribution of pollutants (gases and particle matters) in the urban area, which instead is essential for many purposes (for example for identifying sources of pollution and understanding their impact and behavior). For instance, in the city of Florence (Italy), the regional network consists of 6 stations: 2 urban-traffic ones, 3 background-stations, and one rural-background station as shown in Figure 1. The main reason for using few sensors is represented by the cost; indeed, traditional air pollutant analyzers are complicated, bulky and expensive, each instrument costing anywhere from

¹Carbon dioxide is a natural component of the atmosphere so it is not properly classified as a pollutant but as a climate-changing gas (or greenhouse gas).

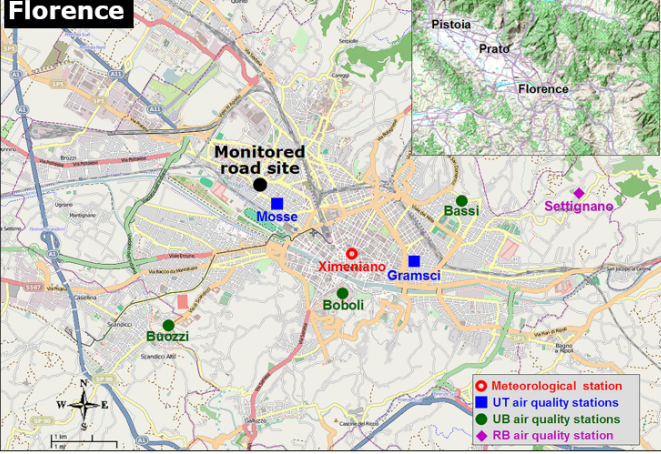


Fig. 1: Florence official air quality monitoring network.

about five to tens of thousands Euro, accompanied by a significant amount of resources required to routinely maintain and calibrate them. However, fine resolution and air pollution data would serve as a powerful resource for understanding the pollution exposure levels and strategies to deal with them. For this purpose, low-cost air quality sensors are an emerging technology and are now commercially available in a wide variety of designs and capabilities. In fact, the recent breakthrough of wireless sensor network technology opens the door to the possibility of cost-effectively monitoring the concentration of pollutants via deployment of multiple low-cost sensors on the area of interest. Such information can be further integrated with the one on traffic-induced air pollution, which indirectly comes from real-time urban traffic monitoring systems, like the ones recently made available by the use of GPS devices (for instance equipped on cellular and smart phones) as probe sensors for traffic flow.

This work has focused on the study and development of an innovative air quality monitoring system able to monitor in real-time the concentration of pollutants (gases and particle matters) in a complex urban environment by processing and fusing data coming from different sources of information, including: point-wise measurements of pollutant concentration and of relevant meteorological variables (such as wind speed, temperature, and humidity) collected from wireless sensors strategically deployed in known locations over the area of interest; and aggregated data on the traffic flow provided by a real-time traffic monitoring system. In the next sections, all the steps followed in the development of the proposed air quality monitoring system will be described in some details. The developed monitoring systems has been validated on different scenarios involving both simulated and real data, collected in two different measurement campaigns.

The rest of this paper is organized as follows. Section 2 describes the adopted mathematical model of air pollutant diffusion and its discrete approximation based on the Finite Element Method (FEM). Section 3 presents the data assimilation techniques used to correct the simulated model on the basis of the available measurements. Section 4 discusses the construction of the simulator of air pollutant diffusion as

well as the methodology used for calculating the emissions associated with city traffic. Section 5 presents the air quality sensors used in the two measurement campaigns described in Section 6. The results obtained with the developed air quality monitoring system in both simulated and real scenarios are provided in Sections 7 and 8, respectively. Finally, concluding remarks are given in Section 9.

II. AIR POLLUTION MODELING

A. Advection-diffusion-reaction model

The diffusion of a pollutant in the environment can be described by a PDE of the form

$$\frac{\partial x}{\partial t} + \mathcal{A}(x) = f \quad \text{in } \Omega \quad (1)$$

with possibly inhomogeneous boundary condition

$$\mathcal{B}(x) = g \quad \text{on } \partial\Omega. \quad (2)$$

where: $x(\mathbf{p}, t)$ is the space-time dependent scalar field of interest (e.g. concentration, temperature), defined over the space-time domain $\Omega \times \mathbb{R}$; the space domain Ω is supposed to be bounded and with smooth boundary $\partial\Omega$; $\mathbf{p} \in \Omega$ denotes the d -dimensional ($d \in \{1, 2, 3\}$) position vector; $t \in \mathbb{R}$ denotes time; $\mathcal{A}(\cdot)$ and $\mathcal{B}(\cdot)$ are the advection-diffusion and, respectively, Robin operators defined as

$$\mathcal{A}(x) = -\lambda \nabla^2 x + \mathbf{v}^T \nabla x$$

and

$$\mathcal{B}(x) = \partial x / \partial \mathbf{n} + \beta x$$

λ is the diffusion coefficient; $\mathbf{v}(\mathbf{p})$ is the advection velocity vector; $\beta(\mathbf{p}) \geq 0$ is a, possibly space-dependent, coefficient; $\partial x / \partial \mathbf{n} = \mathbf{n}^T \nabla x$, \mathbf{n} being the outward pointing unit normal vector of the boundary $\partial\Omega$; $g(\mathbf{p}, t)$ is the forcing term acting on the boundary $\partial\Omega$. The term $f(\mathbf{p}, t)$ represents the internal sources of pollution.

The aim is to estimate the continuous field $x(\mathbf{p}, t)$ given measurements

$$y_{k,i} = x(\mathbf{s}_i(t_k), t_k) + v_{k,i} \quad (3)$$

provided by sensors $i \in \mathcal{S} \triangleq \{1, \dots, S\}$, located at positions $\mathbf{s}_i(t_k) \in \Omega$, at discrete sampling instants t_k , $k \in \mathbb{Z}_+ = \{1, 2, \dots\}$, such that $0 < t_1 < t_2 < \dots$. The sensor positions are allowed to be time-varying in order to account also for mobile sensors.

The above stated dynamic estimation problem is clearly infinite-dimensional. It will be shown in the next section how it can be approximated into a finite-dimensional one by exploiting the *finite element* (FE) method.

B. Finite-element spatial discretization

The PDE (1) with boundary condition (2) can be recast into the following integral form:

$$\int_{\Omega} \frac{\partial x}{\partial t} \varphi d\mathbf{p} - \lambda \int_{\Omega} \nabla^2 x \varphi d\mathbf{p} + \int_{\Omega} \mathbf{v}^T \nabla x \varphi d\mathbf{p} = \int_{\Omega} f \varphi d\mathbf{p}$$

where $\varphi(\mathbf{p})$ is a generic space-dependent weight function. By applying Green's identity and thanks to (2), one obtains:

$$\int_{\Omega} \frac{\partial x}{\partial t} \varphi d\mathbf{p} + \lambda \int_{\Omega} \nabla^T x \nabla \varphi d\mathbf{p} + \int_{\Omega} \mathbf{v}^T \nabla x \varphi d\mathbf{p} - \lambda \int_{\partial\Omega} (g - \beta x) \varphi d\mathbf{p} = \int_{\Omega} f \varphi d\mathbf{p}$$

By subdividing the domain Ω into a suitable set of non overlapping elements and by defining a suitable set of basis functions $\phi_j(\mathbf{p})$, $j = 1, \dots, n$, on them, it is possible to write an approximation of the unknown function $x(\mathbf{p}, t)$ as

$$x(\mathbf{p}, t) = \sum_{j=1}^n \phi_j(\mathbf{p}) x_j(t) = \boldsymbol{\phi}^T(\mathbf{p}) \mathbf{x}(t) \quad (4)$$

where: $x_j(t)$ is the unknown expansion coefficient of function $x(\mathbf{p}, t)$ relative to time t and basis function $\phi_j(\mathbf{p})$; $\boldsymbol{\phi}(\mathbf{p}) \triangleq \text{col}\{\phi_j(\mathbf{p})\}_{j=1}^n$ and $\mathbf{x}(t) \triangleq \text{col}\{x_j(t)\}_{j=1}^n$.

The choices of the basis functions ϕ_j and of the elements are key points of the FE method. Typically, the elements (triangles or quadrilaterals in 2D, polyhedral in 3D) define a FE mesh with vertices $\mathbf{p}_j \in \Omega$, $j = 1, \dots, n$. Then each basis function ϕ_j is a piece-wise polynomial which vanishes outside the FEs around \mathbf{p}_j and such that $\phi_j(\mathbf{p}_i) = \delta_{ij}$, δ_{ij} denoting the Kronecker delta.

By choosing the test function φ equal to the selected basis functions, the Galerkin weighted residual method is applied and the following equation is obtained [13]

$$\underbrace{\left[\int_{\Omega} \boldsymbol{\phi}(\mathbf{p}) \boldsymbol{\phi}^T(\mathbf{p}) d\mathbf{p} \right]}_{\mathbf{M}} \dot{\mathbf{x}}(t) + \underbrace{\left[\lambda \int_{\Omega} \nabla \boldsymbol{\phi}(\mathbf{p}) \nabla \boldsymbol{\phi}^T(\mathbf{p}) d\mathbf{p} \right]}_{\mathbf{S}_{\lambda}} \mathbf{x}(t) + \underbrace{\left[\int_{\Omega} \boldsymbol{\phi}(\mathbf{p}) \mathbf{v}^T(\mathbf{p}) \nabla \boldsymbol{\phi}^T(\mathbf{p}) d\mathbf{p} \right]}_{\mathbf{G}} \mathbf{x}(t) + \underbrace{\left[\lambda \int_{\partial\Omega} \beta(\mathbf{p}) \boldsymbol{\phi}(\mathbf{p}) \boldsymbol{\phi}^T(\mathbf{p}) d\mathbf{p} \right]}_{\mathbf{Q}_{\beta}} \mathbf{x}(t) = \underbrace{\left[\int_{\Omega} \boldsymbol{\phi}(\mathbf{p}) \boldsymbol{\phi}(\mathbf{p})^T d\mathbf{p} \right]}_{\mathbf{Q}_f} \mathbf{u}(t) + \underbrace{\left[\lambda \int_{\partial\Omega} \boldsymbol{\phi}(\mathbf{p}) \boldsymbol{\phi}^T(\mathbf{p}) d\mathbf{p} \right]}_{\mathbf{Q}_g} \mathbf{g}(t) \quad (5)$$

where in the integrals on the contour $\partial\Omega$ it is assumed that the various functions are the restrictions to $\partial\Omega$ of the original functions defined over Ω , and that for $f(\mathbf{p}, t)$ and $g(\mathbf{p}, t)$ expansions akin to (4) hold, i.e.

$$\begin{aligned} g(\mathbf{p}, t) &= \sum_{j=1}^n \phi_j(\mathbf{p}) g_j(t) = \boldsymbol{\phi}^T(\mathbf{p}) \mathbf{g}(t) \\ f(\mathbf{p}, t) &= \sum_{j=1}^n \phi_j(\mathbf{p}) f_j(t) = \boldsymbol{\phi}^T(\mathbf{p}) \mathbf{f}(t) \end{aligned}$$

It is evident how all integrals in the LHS (5) depend only on basis functions and can be computed *a priori*. In particular, the first two integrals yields the well known *mass* and *stiffness*

matrices \mathbf{M} and \mathbf{S}_{λ} [13]. Matrices \mathbf{G} , \mathbf{Q}_{β} , \mathbf{Q}_f , and \mathbf{Q}_g are non standard but can be easily computed in simplex coordinates for first order triangular elements [13], [14].

Then, by regularly discretizing in time (5) with sampling interval Δ (i.e. $t_k = k\Delta$) and approximating the time derivative with the finite difference $\dot{\mathbf{x}}(t) \simeq (\mathbf{x}_{k+1} - \mathbf{x}_k)/\Delta$, the following discrete-time linear descriptor system is obtained:

$$\mathbf{M} \left(\frac{\mathbf{x}_{k+1} - \mathbf{x}_k}{\Delta} \right) + \mathbf{S}_{\lambda} \mathbf{x}_{k+1} + \mathbf{G} \mathbf{x}_{k+1} + \mathbf{Q}_{\beta} \mathbf{x}_{k+1} \simeq \mathbf{Q}_f \mathbf{f}_{k+1} + \mathbf{Q}_g \mathbf{g}_{k+1} \quad (6)$$

which can be rewritten as

$$\left(\mathbf{S} + \frac{\mathbf{M}}{\Delta} \right) \mathbf{x}_{k+1} = \frac{\mathbf{M}}{\Delta} \mathbf{x}_k + \mathbf{u}_k + \mathbf{w}_k \quad (7)$$

where $\mathbf{S} = \mathbf{S}_{\lambda} + \mathbf{G} + \mathbf{Q}_{\beta}$, $\mathbf{u}_k = \mathbf{Q}_f \mathbf{f}_{k+1} + \mathbf{Q}_g \mathbf{g}_{k+1}$ and \mathbf{w}_k is a process disturbance taking into account also the space-time discretization errors. From (11), one obtains the discrete-time model

$$\mathbf{x}_{k+1} = \mathbf{A} \mathbf{x}_k + \mathbf{B} \mathbf{u}_k + \mathbf{B} \mathbf{w}_k \quad (8)$$

where

$$\mathbf{A} = \left(\mathbf{S} + \frac{\mathbf{M}}{\Delta} \right)^{-1} \frac{\mathbf{M}}{\Delta}, \quad \mathbf{B} = \left(\mathbf{S} + \frac{\mathbf{M}}{\Delta} \right)^{-1}.$$

Remark 1: Notice that in the case of Dirichlet boundary conditions of the form $x = g$ on $\partial\Omega$, equations analogous to (11) and (12) can be obtained provided that \mathbf{S} and \mathbf{u}_k are suitably redefined. Further, the considered model can be easily extended so as to account for the presence of a reactive term in the linear operator $\mathcal{A}(x)$ and for space-time dependent diffusion coefficient λ , giving rise to the general model $\mathcal{A}(x) = -\nabla \cdot (\lambda \nabla x) + \mathbf{v}^T \nabla x + rx$.

Clearly, in the above model, the following elements and parameters have to be specified:

- The geometry on which the Finite Element Method (FEM) method is applied, i.e. the domain Ω and the mesh nodes \mathbf{p} , must be chosen both to define the models and plan the measurement campaigns.
- The forcing term f and the boundary values g , that determine the values of \mathbf{u}_k must be tuned according to the vehicle emission rates and the pollutant concentration on the boundary nodes.
- The value of the diffusion coefficient λ for various pollutants can be taken from the literature [12].
- The advection vector \mathbf{v} , representing the wind velocity, can be found for any geographical area in Italy from the web site source [ilmeteo.it](#).

The construction of the considered model is described in some details in Section 4.

In accordance with the above-described model, let $\mathcal{S}_k \subseteq \mathcal{S}$ be the subset of sensors collecting a measurement at the discrete-time instant t_k , then the measurement equation takes the form

$$\mathbf{y}_k = \mathbf{C}_k \mathbf{x}_k + \mathbf{v}_k \quad (9)$$

where,

$$\mathbf{y}_k \triangleq \text{col} \{y_{k,i}\}_{i \in \mathcal{S}_k}, \quad \mathbf{v}_k \triangleq \text{col} \{v_{k,i}\}_{i \in \mathcal{S}_k}, \\ \mathbf{C}_k = \text{col} \left\{ \phi^T(\mathbf{s}_i(t_k)) \right\}_{i \in \mathcal{S}_k}$$

C. Time-discretization

Then, by regularly discretizing in time (5) with sampling interval Δ (i.e. $t_k = k\Delta$) and approximating the time derivative with the finite difference $\dot{\mathbf{x}}(t) \simeq (\mathbf{x}_{k+1} - \mathbf{x}_k)/\Delta$, the following discrete-time linear descriptor system is obtained:

$$\mathbf{M} \left(\frac{\mathbf{x}_{k+1} - \mathbf{x}_k}{\Delta} \right) + \mathbf{S}_\lambda \mathbf{x}_{k+1} + \mathbf{G} \mathbf{x}_{k+1} + \mathbf{Q}_\beta \mathbf{x}_{k+1} \simeq \mathbf{Q}_f \mathbf{f}_{k+1} + \mathbf{Q}_g \mathbf{g}_{k+1}$$

which can be rewritten as

$$\left(\mathbf{S} + \frac{\mathbf{M}}{\Delta} \right) \mathbf{x}_{k+1} = \frac{\mathbf{M}}{\Delta} \mathbf{x}_k + \mathbf{u}_k + \mathbf{w}_k \quad (11)$$

where $\mathbf{S} = \mathbf{S}_\lambda + \mathbf{G} + \mathbf{Q}_\beta$, $\mathbf{u}_k = \mathbf{Q}_f \mathbf{f}_{k+1} + \mathbf{Q}_g \mathbf{g}_{k+1}$ and \mathbf{w}_k is a process disturbance taking into account also the space-time discretization errors. From (11), one obtains the discrete-time model

$$\mathbf{x}_{k+1} = \mathbf{A} \mathbf{x}_k + \mathbf{B} \mathbf{u}_k + \mathbf{B} \mathbf{w}_k \quad (12)$$

where

$$\mathbf{A} = \left(\mathbf{S} + \frac{\mathbf{M}}{\Delta} \right)^{-1} \frac{\mathbf{M}}{\Delta}, \quad \mathbf{B} = \left(\mathbf{S} + \frac{\mathbf{M}}{\Delta} \right)^{-1}.$$

Remark 2: Notice that in the case of Dirichlet boundary conditions of the form $x = g$ on $\partial\Omega$, equations analogous to (11) and (12) can be obtained provided that \mathbf{S} and \mathbf{u}_k are suitably redefined. Further, the considered model can be easily extended so as to account for the presence of a reactive term in the linear operator $\mathcal{A}(x)$ and for space-time dependent diffusion coefficient λ , giving rise to the general model $\mathcal{A}(x) = -\nabla \cdot (\lambda \nabla x) + \mathbf{v}^T \nabla x + rx$.

Clearly, in the above model, the following elements and parameters have to be specified:

- The geometry on which the Finite Element Method (FEM) method is applied, i.e. the domain Ω and the mesh nodes \mathbf{p} , must be chosen both to define the models and plan the measurement campaigns.
- The forcing term f and the boundary values g , that determine the values of \mathbf{u}_k must be tuned according to the vehicle emission rates and the pollutant concentration on the boundary nodes.
- The value of the diffusion coefficient λ for various pollutants can be taken from the literature [12].
- The advection vector \mathbf{v} , representing the wind velocity, can be found for any geographical area in Italy from the web site ilmeteo.it.

The construction of the considered model is described in some details in Section 4.

In accordance with the above-described model, let $\mathcal{S}_k \subseteq \mathcal{S}$ be the subset of sensors collecting a measurement at the discrete-time instant t_k , then the measurement equation takes the form

$$\mathbf{y}_k = \mathbf{C}_k \mathbf{x}_k + \mathbf{v}_k \quad (13)$$

where,

$$\mathbf{y}_k \triangleq \text{col} \{y_{k,i}\}_{i \in \mathcal{S}_k}, \quad \mathbf{v}_k \triangleq \text{col} \{v_{k,i}\}_{i \in \mathcal{S}_k}, \\ \mathbf{C}_k = \text{col} \left\{ \phi^T(\mathbf{s}_i(t_k)) \right\}_{i \in \mathcal{S}_k}$$

D. Use of meteo and vehicular traffic data for parameter tuning and emissions calculation

In a complex scenario such as a modern urban center, the main contribution to pollution is certainly due to city traffic. Traffic-related air pollution is a serious problem with significant health impacts in both urban and suburban environments. Hot emissions are the emissions produced when the engine and the pollution control systems of the vehicle (e.g. catalyst) have reached their normal operating temperature. Following [1], they can be calculated if the emission per unit of activity and the total activity over the reference time scale are known, using the formula:

$$E_{hot} = e \cdot m \quad (14)$$

where: E_{hot} is the hot emission factor, in units of mass per unit of time (usually in $[g \cdot \text{veh}/h]$); e is the emission factor in $[g/km]$; m is the activity, in distance travelled per time unit (usually in $[km \cdot \text{veh}/h]$).

The activity m required for the emission calculation according to equation (14) is defined as:

$$m = n \cdot l \quad (15)$$

where: n is the number of vehicles in each vehicle category; l is the average speed of the amount of vehicles in each vehicle category, on each type of road.

Combining equations (14) and (15), and taking into account the different vehicle categories and the different types of road, the final equation for hot emission estimation can be derived for each type of pollutant:

$$E_k = \sum_{i=1}^{n_c} n_i l_i \sum_{j=1}^{n_p} p_{i,j} e_{i,j,k} \quad (16)$$

where: k identifies the pollutant; i identifies the vehicle category; j identifies the type of road; n_i is the number of vehicles in category i ; l_i is the average speed of vehicle in category i ; $p_{i,j}$ is the percentage of vehicles in each category i , travelling on road type j ; $e_{i,j,k}$ is the emission factor of pollutant k corresponding to the average speed on road type j , for vehicle category i ; n_c is the number of vehicle categories; n_p is the number of road types.

In an urban area the streets can be considered of the same type (i.e. urban road). Moreover, for the activity (16), the following equivalence holds

$$n \cdot l = h \cdot d \quad (17)$$

where: h is the vehicle flow on each type of road; d is the total length of all roads belonging to a certain category of road types.

Then, (16) can be written in the following, simplified form:

$$E_k = d \sum_{i=1}^{n_c} h_i p_i e_{i,k} \quad (18)$$

Vehicle class	Cylinder capacity	Speed range	CO ₂ emission factor (g/km)	R ²
PRE ECE	CC < 1.4 l	10-130	768 + 3.13V - 199ln(V)	-
	1.4 l < CC < 2.0 l	10-130	1005 + 4.15V - 263ln(V)	-
	CC > 2.0 l	10-130	1498 + 8.21V - 0.0133V ² - 421ln(V)	-
ECE 15-00/01	CC < 1.4 l	10-130	173 - 2.52V + 0.0182V ² + 1930/V	-
	1.4 l < CC < 2.0 l	10-130	1065 + 4.00V - 284 ln(V)	-
	CC > 2.0 l	10-130	835 + 3.71V + 2297/V - 229ln(V)	-
ECE 15-02	CC < 1.4 l	10-130	345 + 0.0106V ² + 1275/V - 68.6ln(V)	-
	1.4 l < CC < 2.0 l	10-130	835 + 3.93V + 986/V - 231ln(V)	-
	CC > 2.0 l	10-130	879 + 4.32V + 2298/V - 244ln(V)	-
ECE 15-03	CC < 1.4 l	10-130	664 + 2.09V + 0.00449V ² - 167ln(V)	-
	1.4 l < CC < 2.0 l	10-130	1074 + 5.49V - 0.00461V ² - 305ln(V)	-
	CC > 2.0 l	10-130	957 + 4.51V + 1832/V - 264ln(V)	-
ECE 15-04	CC < 1.4 l	10-130	614 + 2.56V - 157ln(V)	-
	1.4 l < CC < 2.0 l	10-130	264 + 0.0103V ² + 2049/V - 49.8ln(V)	-
	CC > 2.0 l	10-130	1173 + 4.83V - 315ln(V)	-
Improved conventional	CC < 1.4 l	10-130	226 - 3.91V + 0.0368V ²	-
	1.4 l < CC < 2.0 l	10-130	333 - 6.11V + 0.0518V ²	-
Open Loop	CC < 1.4 l	10-130	238 - 3.67V + 0.0319V ²	-
	1.4 l < CC < 2.0 l	10-130	331 - 5.88V + 0.0499V ²	-
EURO I	CC < 1.4 l	5-130	157 - 2.07V + 0.0172V ² + 1835/V	-
	1.4 l < CC < 2.0 l	5-130	231 - 3.62V + 0.0263V ² + 2526/V	-
	CC > 2.0 l	5-130	294 - 5.50V + 0.0393V ² + 3513/V	-

TABLE I: Courtesy of Transport Research Laboratory (TRL) [1]

Speed dependency of carbon dioxide emission factors for gasoline passenger cars.

where: k identifies the pollutant; i identifies the vehicle category; h_i is the average vehicle flow in the urban roads in category i ; d is the total length of the amount of urban roads in a certain area considered area; $p_{i,j}$ is the percentage of vehicles in each category i ; $e_{i,k}$ is the emission factor of pollutant k corresponding to the average speed on urban road type, for vehicle category i ; n_c is the number of vehicles categories.

Since generally the concentration of the pollutants is expressed in $\mu\text{g}/\text{m}^3$ or in mg/m^3 and each subdomain in road geometry shown in Figure 6 has its own pollutant concentration because of the difference of traffic intensity, the hot emission in each road subsection is calculated as follows:

$$E_{vol,k}^{sub} = \frac{d^{sub}}{vol^{sub}} \sum_{i=1}^{n_c} h_i^{sub} p_i e_{i,k} \quad (19)$$

where d^{sub} is the lenght of the road subsection, h_i^{sub} is its vehicle flow and vol^{sub} is a volume corresponding to the area of the same subsection multiplied by a height dimensioned in the order of tens of meters.

The emission factors have been derived using data from engine test-bed measurements. Each engine has been categorised according to the type of vehicle in which it is used. There are four categories of vehicles chosen to represent the *car fleet* of the city of Florence, available from the ACI (Automobile Club d'Italia) website: *passenger cars*, *trucks* or *heavy goods vehicles* (HGVs), *urban buses* and *mopeds*. The method for calculating the emission factor for the first vehicle category is shown in the Tables I and II and depends on the type of pollutant [1]. For the second and third vehicle category the following formula has been used:

$$\varepsilon_{pc} = K_{pc} + a_{pc}v + b_{pc}v^2 + c_{pc}v^3 + \frac{d_{pc}}{v} + \frac{e_{pc}}{v^2} + \frac{f_{pc}}{v^3} \quad (20)$$

where: ε_{pc} is the emission factor; K_{pc} is a constant; a_{pc} - f_{pc} are coefficients; v is the mean velocity of the vehicle.

Vehicle class	Cylinder capacity	Speed range	CO emission factor (g/km)	R ²
PRE ECE	All categories	10-100	281V ^{0.630}	0.924
	All categories	100-130	0.112V + 4.32	
ECE 15-00/01	All categories	10-50	313V ^{0.760}	0.898
	All categories	50-130	27.22 - 0.406V + 0.0032V ²	0.158
ECE 15-02	All categories	10-60	300V ^{0.97}	0.747
	All categories	60-130	26.260 - 0.440V + 0.0026V ²	0.102
ECE 15-03	All categories	10-20	161.36 - 45.62 ln(V)	0.790
	All categories	20-130	37.92 - 0.680V + 0.00377V ²	0.247
ECE 15-04	All categories	10-60	260.788V ^{0.910}	0.825
	All categories	60-130	14.653 - 0.220V + 0.001163V ²	0.613
Improved conventional	CC < 1.4 l	10-130	14.577 - 0.294V + 0.002478V ²	0.781
	1.4 l < CC < 2.0 l	10-130	8.273 - 0.151V + 0.000957V ²	0.767
Open loop	CC < 1.4 l	10-130	17.882 - 0.377V + 0.002825V ²	0.656
	1.4 l < CC < 2.0 l	10-130	9.446 - 0.230V + 0.002029V ²	0.719
EURO I	CC < 1.4 l	10-130	9.846 - 0.2867V + 0.0022V ²	0.133
	1.4 l < CC < 2.0 l	10-130	9.617 - 0.245V + 0.001729V ²	0.145
	CC > 2.0 l	10-130	12.826 - 0.2955V + 0.00177V ²	0.109

TABLE II: Courtesy of Transport Research Laboratory (TRL) [1]

Speed dependency of CO emission factors for gasoline passenger cars.

	K	a	b	c	d	e	f
CO	1.50	-0.0595	0.00119	-6.16E-6	58.8	0	0
CO ₂	110	0	0	0.000375	8702	0	0
VOC	0.186	0	0	-2.97E-7	61.5	0	0
NO _x	0.508	0	0	3.87E-6	92.5	-77.3	0
PM	0.0506	0	0	1.22E-7	12.5	0	-21.1

TABLE III: Courtesy of Transport Research Laboratory (TRL) [1]

Coefficients of emission functions for heavy goods vehicles with gross vehicle weights from 3.5 to 7.5 tonnes.

As seen in the first category, the values of the coefficients depend again on the type of pollutant, but in this case they depend also on each gross vehicle weight; for this reason it has been assumed HGVs having a gross vehicle weight from 3.5 to 7.5 tons. For HGVs and urban buses the values of the coefficients are shown in Tables III and IV respectively.

Finally, for mopeds, the emission factors are presented in Table V.

As it is clear from the expressions in the tables presented in this section, the calculation of the average speed and the flow of vehicles in each category is required for obtaining the emission factors in urban roads. In this respect, *levels of service (LOS)* to classify the vehicle flow and the average speed have been identified, as shown in Tables VI and VII [3]. This information has been used to define four emission classes, each one associated with a different color, corresponding to a

	K	a	b	c	d	e	f
CO	1.64	0	0	0	132	0	0
CO ₂	679	0	0	-0.00268	9635	0	0
VOC	0.0778	0	0	0	41.2	0	184
NO _x	16.3	-0.173	0	0	111	0	0
PM	0.0694	0	0.000366	-8.71E-6	13.9	0	0

TABLE IV: Courtesy of Transport Research Laboratory (TRL) [1]

Coefficients of emission functions for urban buses.

Mopeds	CO (g/km)	NO _x (g/km)	VOC (g/km)	CO ₂ (g/km)
Uncontrolled	15.0	0.03	9.00	27.3
Controlled Stage 1	9	0.03	5	49.4
Controlled Stage 2	5	0.01	2	65.2

TABLE V: Courtesy of Transport Research Laboratory (TRL) [1]

Emission factors for mopeds.

Level of Service	Controlled-Access Highways	Multilane Rural without Access Control	Two Lane Roadways
A Free-Flow	700 vehicles per hour per lane	720 vehicles per hour per lane	420 vehicles per hour total two-way
B Reasonably Free-Flow	1120 vehicles per hour per lane	1200 vehicles per hour per lane	750 vehicles per hour total two-way
C Operation Stable But Becoming Critical	1640 vehicles per hour per lane	1650 vehicles per hour per lane	1200 vehicles per hour total two-way
D Lower Range of Stable	2015 vehicles per hour per lane	1940 vehicles per hour per lane	1800 vehicles per hour total two-way
E Unstable	2200 vehicles per hour per lane	2200 vehicles per hour per lane	2800 vehicles per hour total two-way
F Forced Flow	Greater than E Limit	Greater than E Limit	Greater than E Limit

TABLE VI: Flow rate limits classified as levels of service.

traffic intensity in the maps provided by the *ArcGis* platform. This application, as shown in Figure 2, yields, in real-time, the traffic intensity of any geographical urban area of the world where this information is represented as a map with four different colors; in ascending order of traffic intensity, respectively, green, yellow, orange and red.

Thus, by associating this information to each subdomain of the road network, an estimation of the emission rate h of each internal node of the mesh shown in Figure 8 has been obtained. In turn, such estimate has been used to construct the vector of internal emissions \mathbf{f}_{k+1} and, hence, the vector of exogenous inputs \mathbf{u}_k in model (11).

III. FINITE-ELEMENT STATE ESTIMATION FOR LARGE-SCALE SYSTEMS

To obtain a good estimate of the pollutant concentration in real-time, a mathematical description that models the transport



Fig. 2: Traffic layer on a *Esri* map available from the ArcGis website, including the polluted area of interest in Novoli, Florence.

dynamics of pollutants is not sufficient. Indeed, all mathematical models are affected by uncertainties of different type with respect to the true system. For this reason, in the environmental monitoring systems a data assimilation component is required, aimed at integrating the basic model with data collected over the field, i.e. the area of interest. Thanks to the finite element approximation described in the previous section, the original infinite-dimensional continuous-time filtering problem can be reduced to a much simpler finite-dimensional (albeit large-scale) discrete time linear filtering problem. The most efficient algorithm used in data assimilation problems, in the case of linear systems such as (12)-(13), is undoubtedly the Kalman filter.

Thanks to the finite element approximation described in the previous section, the original infinite-dimensional continuous-time filtering problem can be reduced to a much simpler finite-dimensional (albeit large-scale) discrete time linear filtering problem. The resulting filter recursion becomes:

$$\begin{aligned} \hat{\mathbf{x}}_{k|k} &= \begin{cases} \hat{\mathbf{x}}_{k|k-1} + \mathbf{L}_k (\mathbf{y}_k - \mathbf{h}(\hat{\mathbf{x}}_{k|k-1})) & \text{if } \mathcal{S}_k \neq \emptyset \\ \hat{\mathbf{x}}_{k|k-1} & \text{otherwise} \end{cases} \\ \mathbf{P}_{k|k} &= \begin{cases} \mathbf{P}_{k|k-1} - \mathbf{L}_k \mathbf{C}_k^T \mathbf{P}_{k|k-1} & \text{if } \mathcal{S}_k \neq \emptyset \\ \mathbf{P}_{k|k-1} & \text{otherwise} \end{cases} \\ \hat{\mathbf{x}}_{k+1|k} &= \mathbf{A} \hat{\mathbf{x}}_{k|k} + \mathbf{B} \mathbf{u}_k \\ \mathbf{P}_{k+1|k} &= \mathbf{A} \mathbf{P}_{k|k} \mathbf{A}^T + \mathbf{Q}_k \end{aligned} \quad (21)$$

where \mathbf{L}_k is the Kalman filter gain

$$\mathbf{L}_k = \mathbf{P}_{k|k-1} \mathbf{C}_k (\mathbf{R}_k + \mathbf{C}_k \mathbf{P}_{k|k-1} \mathbf{C}_k^T)^{-1} \quad (22)$$

used to correct the prediction $\hat{\mathbf{x}}_{k|k-1}$ on the basis of the collected measurements \mathcal{S}_k . Of course the correction is applied only for k such that $\mathcal{S}_k \neq \emptyset$ (i.e., when at least one of the sensors is active). The recursion is initialized from suitable $\hat{\mathbf{x}}_{1|0}$ and $\mathbf{P}_{1|0} = \mathbf{P}_{1|0}^T > \mathbf{0}$. In (21), \mathbf{Q}_k and \mathbf{R}_k denote the covariance matrices of the process noise \mathbf{Bw}_k and, respectively, measurement noise \mathbf{v}_k .

Notice that the process noise \mathbf{w}_k arises from the superposition of several uncertainties and/or perturbations (including, e.g., the FE approximation of the continuous field) so that its whiteness and uncorrelation with the initial state, usually assumed in a stochastic framework, do not hold true in practice. As a result, the Kalman filter algorithm (21)-(22) loses its Bayes optimality but still preserves deterministic

TABLE VII: Courtesy of IOSR Journal of Engineering (IOSRJEN) [3]

Urban speed ranges for different LOS proposed in Indian conditions by neural gas Clustering method.

Urban Street Class	I	II	III	IV
Range of Free Flow	90 to 70 Km/hr	70 to 55 Km/hr	55 to 45 Km/hr	45 to 25 Km/hr
Speed(FFS)	80 Km/hr	60 Km/hr	50 Km/hr	35 Km/hr
LOS	Average Travel Speed(Km/hr)			
A	>60	>52	>50	>40
B	>47-60	>37-52	>30-50	>29-40
C	>40-47	>27-37	>23-30	>22-29
D	>33-40	>22-27	>16-23	>15-22
E	>25-33	>16-22	>11-16	>10-15
F	≤25	≤16	≤11	≤10

least-squares optimality as the minimizer of the following cost function

$$\begin{aligned} J = & (\mathbf{x} - \hat{\mathbf{x}}_{1|0})^T \mathbf{P}_{1|0}^{-1} (\mathbf{x} - \hat{\mathbf{x}}_{1|0}) + \\ & \sum_{i=1}^{k-1} (\mathbf{x}_{i+1} - \mathbf{A}\mathbf{x}_i)^T \mathbf{Q}_i^{-1} (\mathbf{x}_{i+1} - \mathbf{A}\mathbf{x}_i) + \\ & \sum_{i=1}^k (\mathbf{y}_i - \mathbf{C}\mathbf{x}_i)^T \mathbf{R}_i^{-1} (\mathbf{y}_i - \mathbf{C}\mathbf{x}_i) \end{aligned}$$

A. Ensemble Kalman Filter

The problem of the Kalman filter described in the previous section is the computational cost necessary to carry out real-time environmental monitoring activities that imply large data processing and consequently high computational costs. In fact, as will be detailed in Section 4, the state space model (12)-(13) arising from the space-time discretization of the original PDE is a large-scale system involving thousands of state variables. For this reason, to process all the data and generate the estimates, we have used a variant of the Kalman filter known as *ensemble Kalman filter* (EnKF), able to provide a substantial reduction of the computational burden while retaining good filtering performance.

The ensemble Kalman filter (EnKF) is a suboptimal estimator, where the error statistics are predicted by using Monte Carlo or ensemble integration. The EnKF method is presented in three stages. First, to represent the error statistics in the forecast step, we assume that at time k , we have an ensemble of q forecasted state estimates with random sample errors. We denote this ensemble as $\mathbf{X}_k^f \in \mathbb{R}^{n \times q}$, where

$$\mathbf{X}_k^f \triangleq (\mathbf{x}_k^{f_1}, \dots, \mathbf{x}_k^{f_q}), \quad (23)$$

and the superscript f_i refers to the i -th forecast ensemble member. Then, the ensemble mean $\bar{\mathbf{x}}_k^f \in \mathbb{R}^n$ is defined as

$$\bar{\mathbf{x}}_k^f \triangleq \frac{1}{q} \sum_{i=1}^q \mathbf{x}_k^{f_i}. \quad (24)$$

Since the true state \mathbf{x}_k is not known, we approximate the estimation error statistics by using the ensemble members. We define the ensemble error matrix $\mathbf{E}_k^f \in \mathbb{R}^{n \times q}$ around the ensemble mean as

$$\mathbf{E}_k^f \triangleq [\mathbf{x}_k^{f_1} - \bar{\mathbf{x}}_k^f, \dots, \mathbf{x}_k^{f_q} - \bar{\mathbf{x}}_k^f] \quad (25)$$

and the ensemble of output error $\mathbf{E}_{y_k}^f \in \mathbb{R}^{p \times q}$ by

$$\mathbf{E}_{y_k}^f \triangleq [\mathbf{y}_k^{f_1} - \bar{\mathbf{y}}_k^f, \dots, \mathbf{y}_k^{f_q} - \bar{\mathbf{y}}_k^f]. \quad (26)$$

We then approximate \mathbf{P}_k^f by $\hat{\mathbf{P}}_k^f$, $\mathbf{P}_{xy_k}^f$ by $\hat{\mathbf{P}}_{xy_k}^f$ and $\mathbf{P}_{yy_k}^f$ by $\hat{\mathbf{P}}_{yy_k}^f$, respectively, where

$$\begin{aligned} \hat{\mathbf{P}}_k^f &\triangleq \frac{1}{q-1} \sum_{i=1}^q \mathbf{E}_k^f (\mathbf{E}_k^f)^T, \\ \hat{\mathbf{P}}_{xy_k}^f &\triangleq \frac{1}{q-1} \sum_{i=1}^q \mathbf{E}_k^f (\mathbf{E}_{xy_k}^f)^T, \quad \hat{\mathbf{P}}_{yy_k}^f \triangleq \frac{1}{q-1} \sum_{i=1}^q \mathbf{E}_{y_k}^f (\mathbf{E}_{y_k}^f)^T \end{aligned} \quad (27)$$

Thus, we interpret the forecast ensemble mean as the best forecast estimate of the state, and the spread of the ensemble

members around the mean as the error between the best estimate and the actual state.

The second step is the analysis step to be performed whenever $\mathcal{S}_k \neq \emptyset$: to obtain the analysis estimates of the state, the EnKF performs an ensemble of parallel data assimilation cycles, where for $i = 1, \dots, q$

$$\mathbf{x}_k^{a_i} = \mathbf{x}_k^{f_i} + \hat{\mathbf{L}}_k (\mathbf{y}_k^i - \mathbf{C}_k \mathbf{x}_k^{f_i}). \quad (28)$$

The *perturbed observations* \mathbf{y}_k^i are given by

$$\mathbf{y}_k^i = \mathbf{y}_k + \mathbf{v}_k^i, \quad (29)$$

where \mathbf{v}_k^i is a zero-random variable with a normal distribution and covariance \mathbf{R}_k . The sample error covariance matrix computed from the \mathbf{v}_k^i converges to \mathbf{R}_k as $q \rightarrow \infty$. We approximate the analysis error covariance \mathbf{P}_k^a by $\hat{\mathbf{P}}_k^a$, where

$$\hat{\mathbf{P}}_k^a \triangleq \frac{1}{q-1} \sum_{i=1}^q \mathbf{E}_k^a (\mathbf{E}_k^a)^T, \quad (30)$$

and \mathbf{E}_k^a is defined by (25) with $\mathbf{x}_k^{f_i}$ replaced by $\mathbf{x}_k^{a_i}$ and $\bar{\mathbf{x}}_k^f$ replaced by the mean of the analysis estimate ensemble members. We use the classical Kalman filter gain expression and the approximations of the error covariances to determine the filter gain $\hat{\mathbf{L}}_k$ by

$$\hat{\mathbf{L}}_k = \hat{\mathbf{P}}_{xy_k}^f (\hat{\mathbf{P}}_{yy_k}^f)^{-1}. \quad (31)$$

The last step is the prediction of error statistics in the forecast step:

$$\mathbf{x}_{k+1}^{f_i} = \mathbf{A}\mathbf{x}_k^{a_i} + \mathbf{w}_k^i, \quad (32)$$

where the values \mathbf{w}_k^i are sampled from a normal distribution with average zero and covariance \mathbf{Q}_k . The sample error covariance matrix computed from the \mathbf{w}_k^i converges to \mathbf{Q}_k as $q \rightarrow \infty$.

Concerning equation (32), it is worth noting that computation of the matrix \mathbf{A} involves the inversion of a large scale matrix and hence is prone to numerical errors. Further, while the matrices \mathbf{M} and \mathbf{S} are sparse thanks to the structure of the FEM approximation, the matrix \mathbf{A} loses this desirable property due to the inversion in (II-C). Hence, in practice it is better to avoid computing \mathbf{A} and instead use directly the descriptor model (11) in the computation of the predicted error statistics. Hence, at each time instant and for any i , the following linear system of equations has to be solved with respect to $\mathbf{x}_{k+1}^{f_i}$

$$\left(\mathbf{S} + \frac{\mathbf{M}}{\Delta} \right) \mathbf{x}_{k+1}^{f_i} = \left(\frac{\mathbf{M}}{\Delta} \mathbf{x}_k^{a_i} + \mathbf{u}_k \right) + \mathbf{w}_k^i \quad (33)$$

The resulting filtering recursion is summarized in Algorithm 1.

Remark 3: Note that the Kalman filter recursion involves computation of the predicted covariance $\mathbf{P}_{k+1|k} \in \mathbb{R}^{n \times n}$, which requires $\mathcal{O}(n^3)$ operation where $n = \dim(\mathbf{x})$. On the contrary for the EnKF, only $\hat{\mathbf{P}}_{xy_k}^f$ and $\hat{\mathbf{P}}_{yy_k}^f$ are evaluated, requiring $\mathcal{O}(pqn)$ operation where $p = \dim(\mathbf{y})$. Hence, if $q \ll n$, then the computational burden of evaluating the approximate covariances in the EnKF is much less than the computational burden of determining the covariances in the EKF.

Initial Data: The ensemble size $q > 0$ and the prior estimate $\hat{\mathbf{x}}_{1|0} = \bar{\mathbf{x}}_1^f$.

Initial Step:

Draw the samples $\mathbf{X}_1^f \triangleq (\mathbf{x}_1^{f_1}, \dots, \mathbf{x}_1^{f_q})$ from the prior estimate $\hat{\mathbf{x}}_{1|0}$ such that $\mathbf{x}_1^{f_i} \sim \mathcal{N}(\hat{\mathbf{x}}_{1|0}, \mathbf{Q}_k)$, for $i = 1, \dots, q$,
compute the measurements $\mathbf{y}_1^{f_i} = \mathbf{h}(\mathbf{x}_1^{f_i})$, for $i = 1, \dots, q$,
compute the mean measurement $\bar{\mathbf{y}}_1^f = \frac{1}{q} \sum_{i=1}^q \mathbf{y}_1^{f_i}$,
compute the prior ensemble matrices \mathbf{E}_1^f and $\mathbf{E}_{y_1}^f$.

for $k = 1, 2, \dots$ **do:**

Step 1 (Correction step):

set $\hat{\mathbf{P}}_{xy_k}^f = \frac{1}{q-1} \sum_{i=1}^q \mathbf{E}_k^f (\mathbf{E}_{y_k}^f)^T$,
set $\hat{\mathbf{P}}_{yy_k}^f = \frac{1}{q-1} \sum_{i=1}^q \mathbf{E}_{y_k}^f (\mathbf{E}_{y_k}^f)^T$,
set $\hat{\mathbf{L}}_k = \hat{\mathbf{P}}_{xy_k}^f (\hat{\mathbf{P}}_{yy_k}^f)^{-1}$,
draw $\mathbf{v}_k^i \sim \mathcal{N}(0, \mathbf{R}_k)$, for $i = 1, \dots, q$,
set $\mathbf{x}_k^{a_i} = \mathbf{x}_k^{f_i} + \hat{\mathbf{L}}_k (\mathbf{y}_k + \mathbf{v}_k^i - \mathbf{C}_k \mathbf{x}_k^{f_i})$, for
 $i = 1, \dots, q$, (data update)
set $\hat{\mathbf{x}}_{k|k} \triangleq \bar{\mathbf{x}}_k^a = \frac{1}{q} \sum_{i=1}^q \mathbf{x}_k^{a_i}$,
set $\mathbf{E}_k^a = [\mathbf{x}_k^{a_1} - \bar{\mathbf{x}}_k^a, \dots, \mathbf{x}_k^{a_q} - \bar{\mathbf{x}}_k^a]$, (optional)
set $\hat{\mathbf{P}}_k^a = \frac{1}{q-1} \sum_{i=1}^q \mathbf{E}_k^a (\mathbf{E}_k^a)^T$, (optional)

Step 2 (Prediction step):

draw $\mathbf{w}_k^i \sim \mathcal{N}(0, \mathbf{Q}_k)$, for $i = 1, \dots, q$,
compute $\mathbf{x}_{k+1}^{f_i}$ by solving the system of linear equations
 $i = 1, \dots, q$,
 $\left(\mathbf{S} + \frac{\mathbf{M}}{\Delta} \right) \mathbf{x}_{k+1}^{f_i} = \left(\frac{\mathbf{M}}{\Delta} \mathbf{x}_k^{a_i} + \mathbf{u}_k \right) + \mathbf{w}_k^i$, for
set $\hat{\mathbf{x}}_{k+1|k} \triangleq \bar{\mathbf{x}}_{k+1}^f = \frac{1}{q} \sum_{i=1}^q \mathbf{x}_{k+1}^{f_i}$,
set $\mathbf{E}_{k+1}^f = [\mathbf{x}_{k+1}^{f_1} - \bar{\mathbf{x}}_{k+1}^f, \dots, \mathbf{x}_{k+1}^{f_q} - \bar{\mathbf{x}}_{k+1}^f]$,
set $\mathbf{y}_{k+1}^{f_i} = \mathbf{C}_{k+1} \mathbf{x}_{k+1}^{f_i}$, for $i = 1, \dots, q$,
set $\bar{\mathbf{y}}_{k+1}^f = \frac{1}{q} \sum_{i=1}^q \mathbf{y}_{k+1}^{f_i}$,
set $\mathbf{E}_{y_{k+1}}^f = [\mathbf{y}_{k+1}^{f_1} - \bar{\mathbf{y}}_{k+1}^f, \dots, \mathbf{y}_{k+1}^{f_q} - \bar{\mathbf{y}}_{k+1}^f]$.

end for

Algorithm 1: FEM Ensemble Kalman Filter

IV. AIR-QUALITY SENSORS

Recent air quality regulations (Directive 2008/50/EC) enforce the transition from point-based monitoring networks to new tools that must be capable of mapping and forecasting air quality on the totality of land area, and therefore the totality of citizens. This implies that new tools, such as models and additional indicative measurements, are needed in addition to accurate fixed air quality monitoring stations, that until now have been taken as reference by local administrators for the enforcement of various mitigation strategies. However, due to their sporadic spatial distribution, they cannot describe the high spatial pollutant variations within cities. Integrating additional indicative measurements may provide adequate information on the spatial distribution of air quality parameters. For this purpose, new low-cost and small size sensors are becoming available to be employed in air quality



Fig. 3: IP68 box AirQino. The system is provided with an internal DC-DC converter unit that accepts a wide range of voltage inputs, from 10 V dc to 30 V dc.

monitoring including mobile applications. It was precisely the use of this type of sensor that has allowed the acquisition of pollutant concentration measurements in the field to be used later (offline) for data assimilation. In particular we used *AirQino*, a compact low-cost air quality monitoring station by the Institute of Biometeorology-Italian National Research Council (IBIMET-CNR). AirQino is based on an Arduino Shield Compatible electronic board and integrated with low-cost and high resolution industrial *Strain Measurement Devices* (SMD), dedicated to monitoring environmental parameters and air quality pollutants (humidity, temperature, CO, CO₂, O₃, NO₂, VOC, PM2.5, PM10) in urban environment. The board also incorporates a microprocessor unit that acquires all the installed sensor data. Sensors transmit geolocated data through the General Packet Radio Service (GPRS) technology to a data server connected to the applications and web server allowing to display observations in real-time on a web browser [4]. The board is placed into an IP68 waterproof box as shown in Figure 3. Because the gases monitored by the AirQino sensor board includes also reactive ones, airflow inside the waterproof box is designed to minimize the gas interference. Furthermore, a small brushless fan blows the air out of the box. This creates a depression that attracts air from the inlet window.

The sensors installed on the board have a good accuracy, low cost as well as interfacing capabilities and they provide a good tradeoff between cost effectiveness and reliability to ensure the continuity and traceability of observations. The list of sensors with their specifications is reported in Table VIII. The measurement ranges of these sensors are reported in Table IX.

In addition to the IP68 box AirQino (see Figure 3), two other versions have been used in the monitoring work:

- *Indoor AirQino*: used for indoor measurements (see Figure 4a) as explained in Section ?? to allow the evaluation of a mean pollutant concentration within closed places (buildings) and estimate plausible initial condition values.
- *Mobile AirQino*: installed on a special bike (see Figure 4b) developed by the Department of Industrial Engineering of the University of Florence (Italy). This station version includes a Bluetooth module.

In both versions a Bluetooth module is included. To collect data, an Android phone application is provided to manage,

Pollutant	Manufacturer	Model	Type	Output
CO ₂	CO2meter	Senseair S8	Non-dispersive infrared (NDIR)	ppm
O ₃	SGX Sensortech	MiCS-OZ-47	MOS-type gas sensors	ppb
T/RH	Aosong	DHT22	Semiconductor	°C/%
O ₃	SGX Sensortech	MiCS-2614	MOS-type gas sensors	counts
NO ₂	SGX Sensortech	MiCS-2714	MOS-type gas sensors	counts
CO/CH ₄	FIGARO	TGS-2600	MOS-type gas sensors	counts
CO/VOC	SGX Sensortech	MiCS-5524	MOS-type gas sensors	counts
PM2.5/PM10	Novasense	SDS011	Laser scattering	µg/m ³

TABLE VIII: AirQino sensor specifications. The count range 0-1024 is the digital to analog conversion board scale.

Parameter	Reference Unit	Range
T	°C	-40 – 80
Rh	%	0 – 100
CO ₂	ppm	0 – 2000
O ₃	ppb	20 – 200
NO ₂	ppm	0.05 – 5
CO	ppm	1 – 30
PM	µg/m ³	0 – 999
VOC	ppm	1 – 100

TABLE IX: AirQino sensor ranges in reference unit measure.

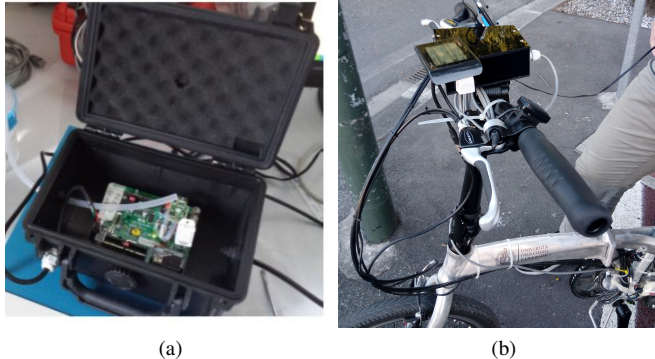


Fig. 4: Indoor AirQino (a) and Mobile AirQino (b).

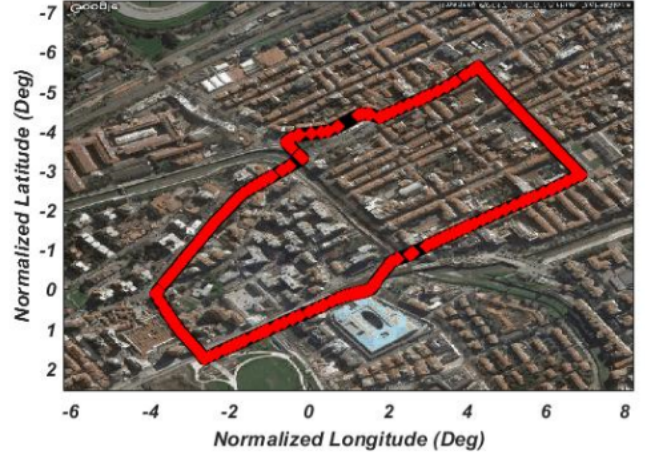


Fig. 5: Boundaries of the area of interest in Novoli, Florence, drawn on a *Google Maps* satellite image.

via Bluetooth, sensor reading and to track the cell phone GPS signal.

V. AIR-QUALITY MONITORING CASE-STUDY

The geographical area chosen for studying the behavior of pollutants is an urban cross-section of the city of Florence, in the Novoli area, limited to the north by *Via di Novoli* and *Via Maragliano*, to the south by *Via Francesco Baracca* and *Via del Ponte alle Mosse*, to the west by *Via Niccolò Paganini* and to the east by *Via Francesco Doni*, as shown in Figure 5. This area has been chosen since it contains two fixed traffic pollution measurement terminals, one located in *Via del Ponte alle Mosse* of ARPAT, and the other one in *Via della Villa Demidoff* of IBIMET-CNR.

Using an online application known as *geojson.io* it has been possible to identify the geographic coordinates of the urban area of interest and import them into the Matlab environment to reconstruct the domain of the area and its geometry. The basic idea has been to subdivide the road network in subdomains about 20 [m] long, so as to allow a high-resolution and simulation capacity for the concentration of pollutants in the various road sections. Using the same method, it has also been possible to reconstruct the 2D-shape of the buildings and the intermediate areas between the road network and buildings, referred to as *background*. The resulting geometry developed in the Matlab environment is shown in Figure 6.

After generating the domain Ω , it has been possible to generate the mesh with its relative elements via the *Partial Differential Equation Toolbox™* (PDE Toolbox) which provides functions for solving partial differential equations in 2D, 3D, and time using finite element analysis. In Figure 8, the mesh nodes \mathbf{p}_i are clearly visible. The parameters concerning the complexity and space resolution of the adopted model for the considered Novoli area are reported in Table X.

VI. SIMULATION RESULTS

In this section, we present the results of the EnKF-based data assimilation algorithm on synthetic data generated from

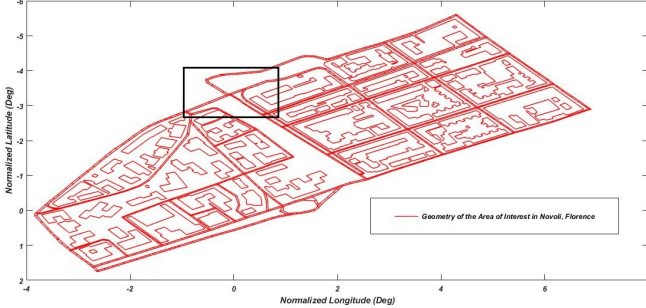


Fig. 6: Geometry of the area of interest in Novoli, Florence, showing streets and buildings. The rectangle with the black border focuses on a cross-section of the geometry (Figure 7), in which it can be seen how the streets have been divided into subsections.

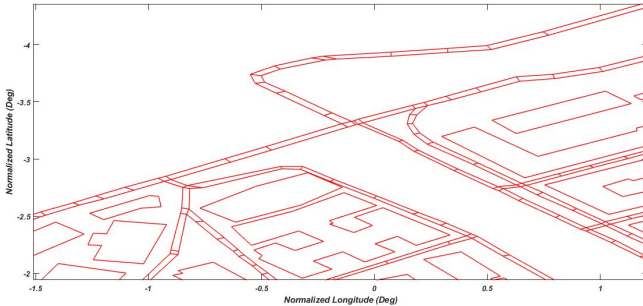


Fig. 7: Cross-section of the geometry of the area of interest. The subsections composing the urban roads are visible.

Number of nodes	28144
Number of elements	55453
Number of edges	12333

TABLE X: Mesh properties.

a simulation scenario modeling the diffusion of CO₂ in the area of interest. The simulated scenario matches the first measurement campaign both in terms of environmental conditions (i.e. traffic flow, diffusivity, wind intensity and direction) and measurement collection (i.e., timing and geographical position of the measurements within the area of interest). This choice makes it possible to evaluate, in a comprehensive way, the capability of the proposed data assimilation algorithm to estimate the concentration field in a realistic scenario by considering the data generated by the simulator as *ground truth* for the filter. The internal emissions used in filter are different from the one used in the simulator, and specifically are obtained from the latter by inserting a random noise. In this way, we can model the fact that, in practice, the true emissions can only be known approximately.

Performance was evaluated by means of two criteria: the Space Averaged Root Mean Square Error (SA-RMSE) and the Time averaged RMSE (TA-RMSE). The SA-RMSE for the state estimate $\hat{\mathbf{x}}_{k|k}$ at time instant k calculated using N_P Monte Carlo simulations is defined as

$$SA\text{-RMSE}(k) \triangleq \sqrt{\frac{1}{N_P n} \sum_{i=1}^{N_P} \tilde{\mathbf{x}}_{k|k}^T(i) \tilde{\mathbf{x}}_{k|k}(i)} \quad (34)$$

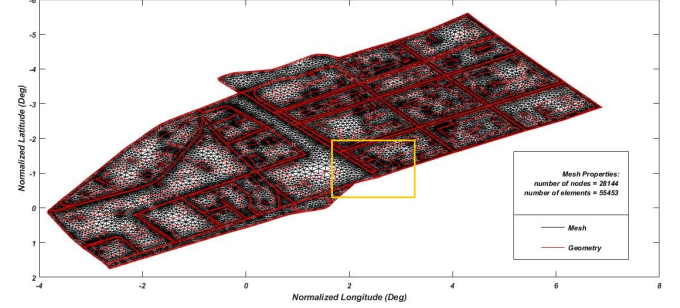


Fig. 8: Mesh extrapolated from the geometry of the area of interest. At this magnification level, the elements of the mesh are almost indistinguishable; conversely the elements are visible at a higher magnification level as shown in Figure 9, where the mesh cross-section within the yellow-bordered box is enlarged.

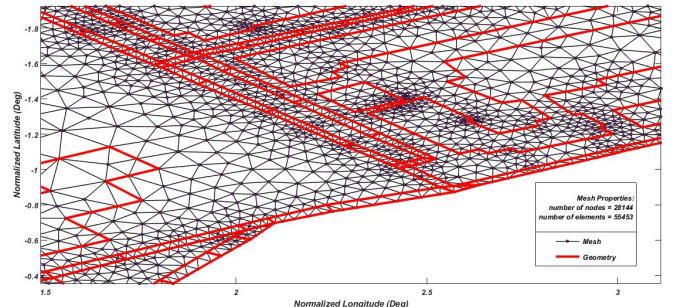


Fig. 9: Cross-section of the mesh shown in Figure 8. At this magnification level the elements are clearly visible.

where $\tilde{\mathbf{x}}_{k|k}(i) = \mathbf{x}_k - \hat{\mathbf{x}}_{k|k}(i)$ is the estimate error and $\hat{\mathbf{x}}_{k|k}(i)$ is the estimate of \mathbf{x}_k relative to the i -th Monte Carlo trial. The TA-RMSE is instead defined as

$$TA\text{-RMSE}(j) \triangleq \sqrt{\frac{1}{N_P N_T} \sum_{i=1}^{N_P} \sum_{k=1}^{N_T} (\tilde{x}_{k|k,j})^2}, \text{ for } j = 1, \dots, n \quad (35)$$

where n is the total number of the mesh nodes, N_T is the total number of time steps, $\tilde{x}_{k|k,j} = x_{k,j} - \hat{x}_{k|k,j}$ and $\hat{x}_{k|k,j}$ is the pollutant concentration estimate of \mathbf{x}_k in the j -th node of the mesh at time instant k . Notice that the SA-RMSE allows one to evaluate how the estimation error varies with time, also as a function of the collected measurements, whereas the TA-RMSE makes it possible to evaluate the uniformity of the estimation error in the domain of interest. Three different tests have been performed by considering an ensemble size of 10, 20, and 50, respectively. In each setting, the SA-RMSE and the TA-RMSE have been computed over 50 Monte Carlo Trials. From the examination of the obtained results, the following general conclusions can be drawn:

- The SA-RMSE decreases with the increase of the ensemble size q as evident from Fig. 10. As expected, in the time interval in which no measurement is collected and, hence, only prediction is performed, the estimation error increases with time. However, as soon as new measurements arrive, the estimation error promptly decreases.

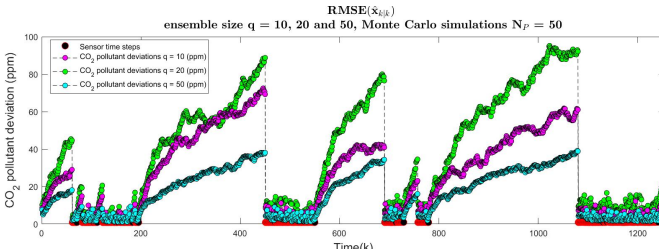


Fig. 10: Performance evaluation on simulated data: time behavior of the SA-RMSE computed over 50 Monte Carlo trials considering three different ensemble sizes. The red points on the abscissas represent the time instants in which a computer-simulated measurement is generated and used by the filter so as to update the estimate.

N_T	$ \mathcal{K} $	σ_q^2	R_k	Δ
1250	422	25^2	3^2	10

TABLE XI: Performance evaluation on simulated data: simulation parameters.

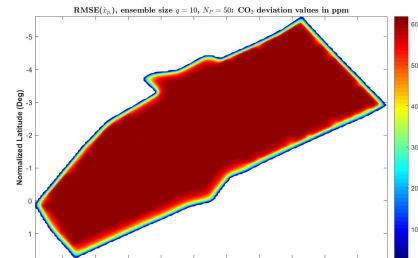
This shows the capability of the proposed algorithm to exploit data assimilation in order to correct the error of the model used in the prediction step.

- The TA-RMSE is uniform all over the domain Ω (see Fig. 10), except on the boundary where such value is null because the CO₂ concentration is considered to be known and used as boundary condition for both the simulator and the filter. This shows the capability of the proposed algorithm to correctly estimate the concentration field even where no measurement is collected (recall that the measurement sampling points are depicted in Fig. ??). Notice that, also in this case, the error decreases as the ensemble size increases.

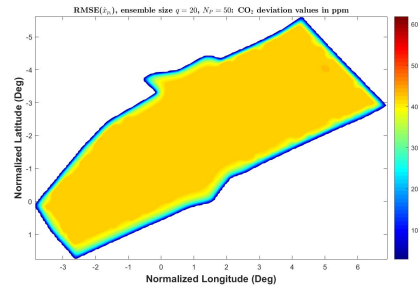
Since both the SA-RMSE and the TA-RMSE cannot be computed for experimental data (being the true concentration field unknown), it is important to consider different evaluation criteria that can be computed without using the true fields and, hence, can be used also for experimental data. For this purpose, one can resort either to regression functions (Fig. 12) or to quantitative criteria comparing the measured (in this case the computer simulated pollutant concentration sample data) with the predicted observations. Specifically, have considered the Prediction RMSE (P-RMSE)

$$P\text{-RMSE}(k) \triangleq \sqrt{\frac{1}{|\mathcal{S}_k|} (\hat{\mathbf{y}}_{k|k-1} - \mathbf{y}_k)^T (\hat{\mathbf{y}}_{k|k-1} - \mathbf{y}_k)}, \quad k$$

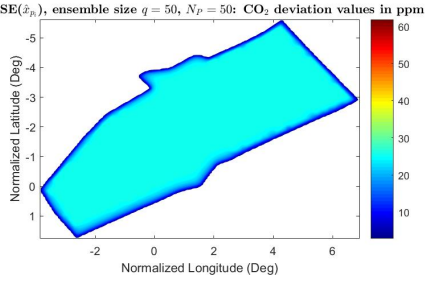
where $\mathcal{K} \subset \mathbb{R}$ is the set of sampling times and \mathcal{S}_k is the set of coordinate points within the domain Ω wherein a measurement is collected at time k . The time behavior of the P-RMSE is shown in Fig. 11. The simulation parameters are shown in Table XI, where σ_q is the process noise standard deviation, i.e. $Q = \mathbf{I}\sigma_q^2$ for all k . The results provided in Figs. 11 and 12 confirm the effectiveness of the proposed data assimilation algorithm,



(c)



(d)



(e)

Fig. 10: Performance evaluation on simulated data: space distribution of the TA-RMSE computed over 50 Monte Carlo trials considering an ensemble size of 10 (a), 20 (b), and 50 (c), respectively.

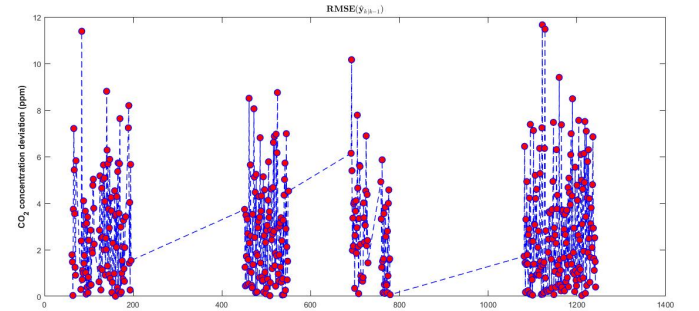


Fig. 11: Performance evaluation on simulated data: time behavior of the P-RMSE between the simulated CO₂ concentration values and the predictions of the data assimilation algorithm. In this simulation, the ensemble size was chosen equal to 150.

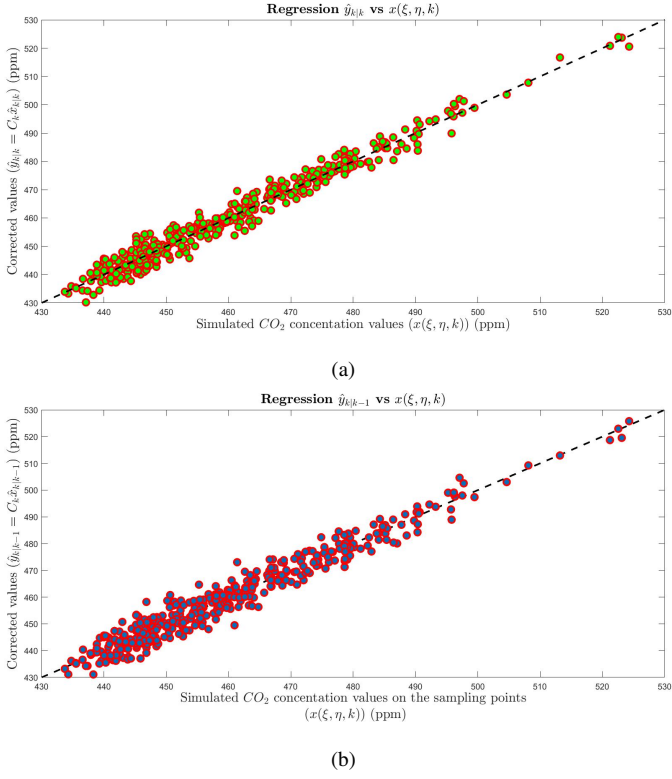


Fig. 12: Performance evaluation on simulated data: regression functions comparing simulated computer CO₂ concentration values and both the corresponding corrections $\hat{y}_{k|k}$, $k \in \mathcal{K}$ (a) and predictions $\hat{y}_{k|k-1}$, $k \in \mathcal{K}$ (b).

We conclude the performance evaluation on the simulated data by comparing the CO₂ concentration field of the simulated model with the estimated field obtained by means of the proposed data assimilation algorithm. Three frames corresponding to three different time instants have been selected and displayed in Figure 13. The big black spot shown into the domain of interest on the estimated field representation is the sampling point of the computer simulated measurement at the considered time instant. From the examination of the obtained results, the following general conclusions can be drawn:

- the estimated field is very close to the simulated one (i.e., the ground truth), hence confirming the effectiveness of the considered data assimilation algorithm;
- the mean CO₂ concentration increases over time because of the increasing emission level due to the traffic flow data collected from the *ArcGis* websource (see Section ??). In fact, the considered time slot coincides with an increase in the level of traffic within the considered urban area;
- Figure 13 shows how the average concentration along the roads is greater than in the background or in buildings where the diffusion coefficient is lower. Furthermore, the CO₂ concentration in the streets is consistent with the traffic flow data collected from the *ArcGis* web platform.

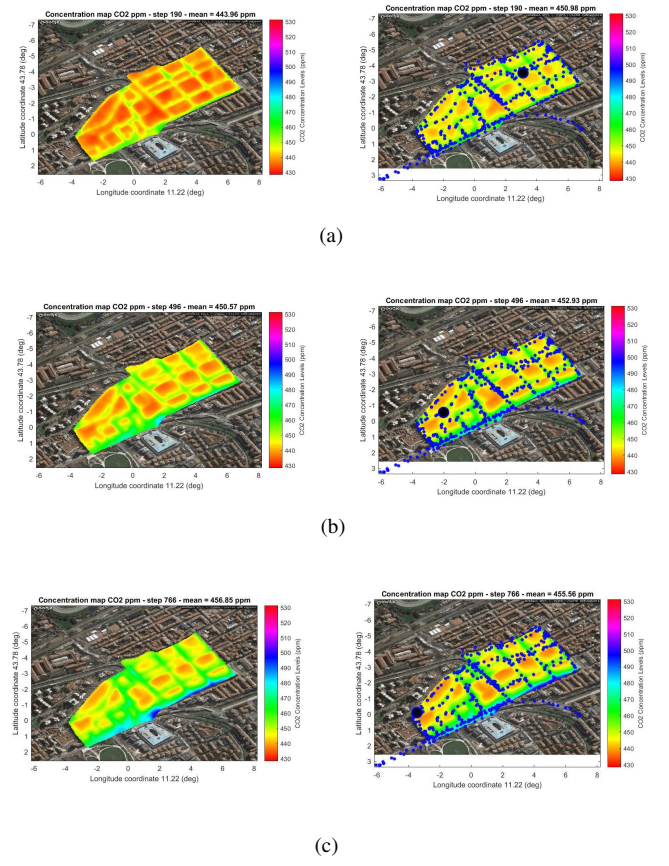


Fig. 13: Performance evaluation on simulated data: 2D comparisons of simulated CO₂ concentration field (left) and estimated field (right) at difference time instants.

N_T	$ \mathcal{K} $	σ_q^2	R_k	Δ
2500	772	25^2	3^2	10

TABLE XII: Parameters used in the data assimilation algorithm for the second measurement campaign.

VII. EXPERIMENTAL RESULTS

In this section, we present experimental results concerning the estimation of the concentration field from the data collected in the two measurement campaigns described in Section 6. For the first measurement campaign, results concerning estimation of CO₂ concentration field in the area of interest are provided, and the parameters used in the filter are the same as those used in the performance evaluation on simulated data of Section 7 (see Table XI); conversely, for the second measurement campaign, we have considered the problem of estimating the CO₂ concentration field and the filter parameters have been chosen as shown in Table XII.

Since, in this case, the true concentration field is unknown the TA-RMSE and SA-RMSE cannot be computed. Hence, the P-RMSE of equation (36) is used as performance criterium in order to evaluate the performance of the data assimilation algorithm. Fig. 16 provides the time behavior of the P-RMSE computed in the scenario corresponding to the first measurement campaign. The P-RMSEs, for each single

sensor as well as considering all the sensors together, in the scenario corresponding to the second measurement campaign are depicted in Fig. 18. The predictions provided by the data assimilation algorithm are also compared with the true measurements by means of regression functions as shown in Figure 15. Finally, the estimated concentration fields of CO₂ (first measurement campaign) and CO (second measurement campaign) pollutants at difference time instants are shown in Figures 19 and 20, respectively. From the examination of the obtained results, the following general conclusions can be drawn:

- From Figs. 16-18, we can observe that the difference between measurements y_k and predictions $\hat{y}_{k|k-1}$ is small. Further, for the first measurement campaign such a difference is comparable to the difference found in the simulated scenario of Section 7. This result indicates that the estimated concentration field allows one to accurately predict the future measurements, and hence the estimates can be considered reliable.
- In both assimilation processes, estimates of pollutant concentration meet expectations. Indeed these values are on average higher along the roads, and smaller in the background or in the buildings.
- The time variation of the pollutant concentration is in good agreement with the observed traffic intensity. For instance, in the second measurement campaign, the concentration is higher at the beginning and the end, and instead lower in the middle segment.

VIII. CONCLUSION

The project has addressed high-resolution air quality monitoring in an urban environment exploiting data assimilation techniques that combine mathematical modeling of the pollutant dispersion dynamics along with pointwise-in-time-and-space pollutant concentration measurements provided by appropriate sensors. In particular, the project has led to the complete software development of a data-assimilation system and to its pilot application to air quality monitoring of a given area in the city of Florence. The developed system exploited the following ingredients: Advection-Diffusion (AD) Partial Differential equation (PDE) for air pollution modeling; Finite Element Method (FEM) for spatial discretization of the AD PDE into a finite-dimensional large-scale continuous-time state-space model; time-discretization to obtain a discrete-time state space model; use of meteo and vehicular traffic data for tuning the model parameters and computing input emissions; Ensemble Kalman Filter (EnKF) for computationally efficient data assimilation with a large-scale model; low-cost mobile and/or fixed AirQino boards, developed by IBIMET-CNR, for measuring concentrations of several pollutants and air temperature as well as radio transmitting geolocated measurements to the data assimilation center. The effectiveness of the system, in terms of accurate space-time reconstruction of the pollutant concentration map, has been successfully tested via both computer-simulated and real data, the latter collected through data-acquisition campaigns with fixed and/or mobile sensors located in the area of interest.

Possible directions for future works are: creation of a network of sensors covering the whole urban area; creation of a network of IMP platforms in critical points in the city so as to combine air quality measurements with measurements of vehicle flows divided by vehicle classes; active involvement of citizens in air quality monitoring (citizen science); real-time strategies for pollution exposure control; automatic control systems for lowering the level of pollution (for example, pollutant suction filters positioned at critical points); intelligent control systems for traffic sorting, regulated by the level of pollution.

ACKNOWLEDGMENT

The authors would like to thank *Fondazione Cassa di Risparmio Firenze* for the financial support of this project; all the people involved in the project and particularly Lin Gao, Suqi Li, and Bailu Wang; Alessandro Zaldei of IBIMET-CNR for providing us the sensors used in the measurement campaigns; Alice Cavaliere, Sara Di Lonardo, and Lapo Frascati for helping with the measurement campaigns.

REFERENCES

- [1] Transport Research Laboratory, *Project Report SE/491/98, Methodology for calculating transport emissions and energy consumption*, Edited by A. J. Hickman.
- [2] P. J. Landrigan, R. Fuller, N. J. Acosta, O. Adeyi, R. Arnold, A. B. Baldé , R. Bertollini, S. Bose-O'Reilly, J. I. Boufford, P. N. Breysse, et al. *The Lancet Commission on pollution and health. The Lancet*, 2017.
- [3] A. K. Das1, A. K. Patnaik, A. N. Dehury, P. K. Bhuyan, U. Chattaraj and M. Panda. Defining Level of Service Criteria of Urban Streets Using Neural Gas Clustering. *IOSR Journal of Engineering (IOSRJEN)*, 3(5):18–25, May, 2013.
- [4] A. Zaldei, F. Camilli, T. De Filippis, F. Di Gennaro, S. Di Lonardo, F. Dini, B. Gioli, G.i Gualtieri, A. Matese, W. Nunziati, et al. An integrated low-cost road traffic and air pollution monitoring platform for next citizen observatories. *Transportation research procedia*, 24:531-538, 2017.
- [5] G. Battistelli, L. Chisci, N. Forti, G. Pelosi, and S. Selleri. Distributed finite-element kalman filter for field estimation. *IEEE Transactions on Automatic Control*, 62(7):3309–3322, 2017.
- [6] Alice Cavaliere. *Low-cost air quality stations and control networks for a smart city*. PhD thesis, University of Florence, 2017.
- [7] Kai Jen Chuang, Yuan Horng Yan, Shu Yi Chiu, and Tsun-Jen Cheng. Longterm air pollution exposure and risk factors for cardiovascular diseases among the elderly in Taiwan. *Occupational and Environmental Medicine*, 1(68):64–68, 2014.
- [8] N. Forti, G. Battistelli, L. Chisci, S. Li, B. Wang, and B. Sinopoli. Distributed joint attack detection and secure state estimation. *IEEE Transactions on Signal and Information Processing over Networks*, 2018.
- [9] Martin J. Gander. Schwarz methods over the course of time. *ETNA. Electronic Transactions on Numerical Analysis*, 31:228–255, 2008.
- [10] Cristina B B Guerreiro, Valentin Foltescu, and Frank De Leeuw. Air quality status and trends in Europe. *Atmospheric environment*, (98):376–384, 2014.
- [11] P.L. Lions. On the Schwarz alternating method. I. In *First Int. Symp. on Domain Decomposition Methods for Partial Differential Equations*, pages 1–142, 1988.
- [12] W. J. Massman. A review of the molecular diffusivities of H₂O, CO₂, CH₄, CO, O₃, SO₂, NH₃, N₂O, NO, and NO₂ in air, O₂ and PN₂ near stp. *Atmospheric Environment*, 32(16):1111–1127, March 1998.
- [13] G. Pelosi, R. Cocciali, and S. Selleri. *Quick finite elements for electromagnetic waves*. Artech House, 2009.
- [14] P.P. Silvester and R.L. Ferrari. *Finite elements for electrical engineers*. Cambridge University Press, 1996.

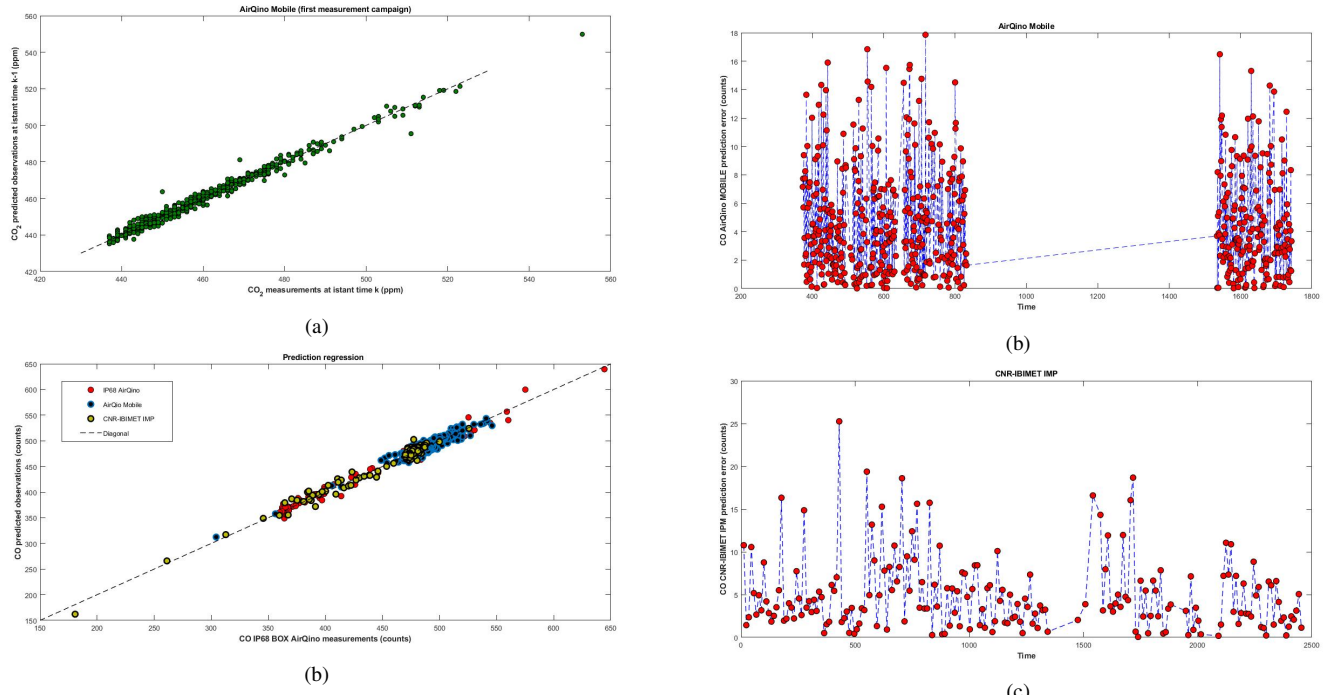


Fig. 15: Measurement campaigns: regression functions comparing the measured pollutant concentration and the corresponding prediction $\hat{y}_{k|k-1}$ in the first (a) and second (b) measurement campaign. For the second measurement campaign the comparison refers to all the three available sensors.

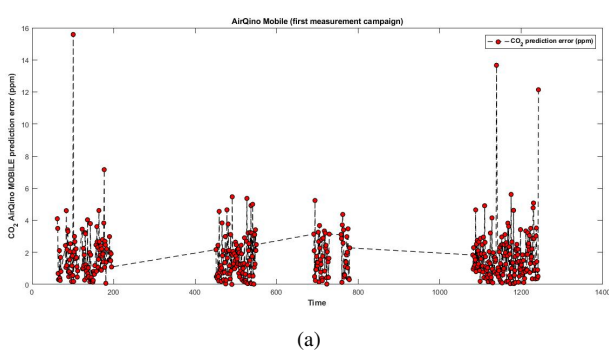


Fig. 16: First measurement campaign: time behavior of the P-RMSE between the measured CO₂ concentration values and the predictions of the data assimilation algorithm.

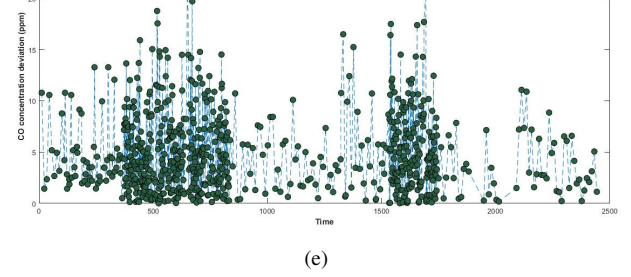


Fig. 18: Second measurement campaign: time behavior of the P-RMSE between the measured CO concentration values and the predictions of the data assimilation algorithm computed for each sensor (a),(b),(c) and considering all the sensors together (d).

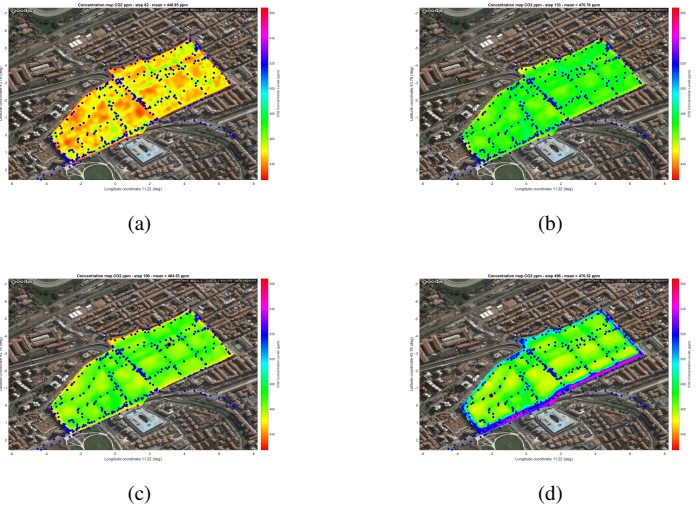


Fig. 19: First measurement campaign: estimated CO₂ concentration field at different time instants.

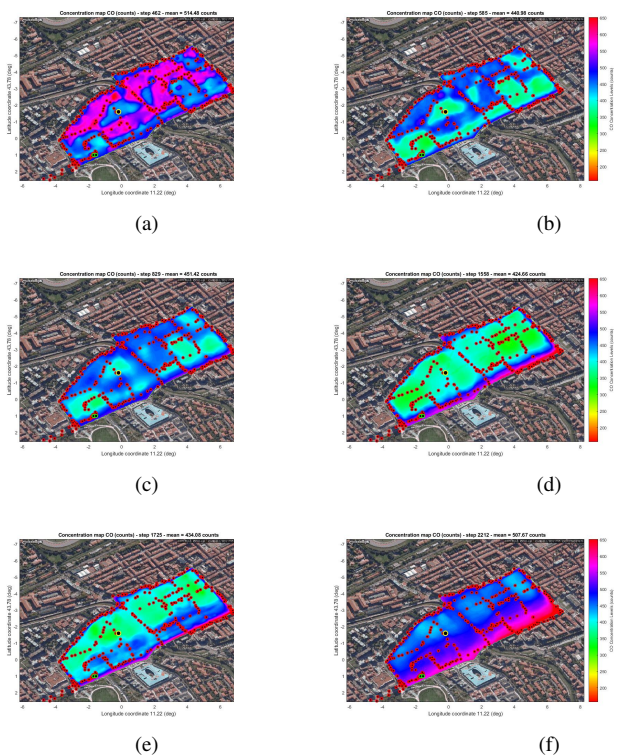


Fig. 20: Second measurement campaign: estimated CO concentration field at different time instants.